X-ray imaging with submicrometer resolution employing transparent luminescent screens

Andreas Koch, Carsten Raven, Per Spanne, and Anatoly Snigirev

European Synchrotron Radiation Facility, BP 220, F-38043 Grenoble, France

Received August 18, 1997; revised manuscript received January 28, 1998; accepted March 9, 1998

Microimaging techniques with synchrotron radiation demand fast, on-line x-ray detectors with a spatial resolution in the micrometer or submicrometer range. For this task an x-ray detector based on a transparent, i.e., nonscattering, luminescent screen has been developed. Its performance is described experimentally and theoretically. The detector consists of an $Y_3Al_5O_{12}$:Ce screen, microscope optics, and a low-noise CCD camera, operated at x-ray energies between 10 and 50 keV. Good image quality is achieved if the depth of focus of the optical system is matched to the x-ray absorption length or thickness of the scintillator. A spatial resolution of 0.8 μm fwhm (1000 line pairs/mm with 10% contrast) was measured by recording the interferogram of a boron fiber. First applications in phase contrast imaging and microtomography are shown. © 1998 Optical Society of America [S0740-3232(98)02507-1]

OCIS codes: 180.7460, 110.7440, 110.6960, 260.3800, 220.4830, 310.6860.

1. INTRODUCTION

Third-generation synchrotron sources offer vast possibilities for different x-ray imaging techniques as a result of high brilliance and coherence of the source. These techniques, such as phase contrast imaging, holography, and microtomography, demand x-ray detectors with a high spatial resolution, preferentially in the micrometer or submicrometer range. Furthermore, since one of the most promising x-ray microimaging techniques is computed microtomography, the need to take several hundred images for a single tomogram calls for fast and on-line working detectors. X-ray energies are typically 5–20 keV for absorption radiography and up to 60 keV in phase contrast imaging.

Spatial resolution of 1 μm with high-energy x rays was achieved, until recently, almost exclusively with x-ray films, the disadvantage being a slow, off-line detector system and a small dynamic range. Even higher resolution, down to 40 nm, was achieved with photoresist for soft x rays ($<$600 eV)[1] but with the same disadvantage of off-line image reconstruction. Electronic detectors, however, allow fast, on-line image acquisition. Charge-coupled devices (CCD's) that are used in direct x-ray detection are limited to a resolution of approximately 6 μm by their pixel size. Detectors based on photocathodes[2] with a thickness of 0.3 μm show very low x-ray absorption at energies between 10 and 60 keV (resolution < 1 μm). Detectors based on photoconductors and electron-beam readouts are potentially of interest because strongly absorbing photoconductors are available (e.g., PbO, CdTe). The thickness of their detection layers can be high while high resolution is preserved, since the signal charge is locally confined by the applied electric fields. A resolution of 500 line pairs/mm (lp/mm) was reported,[3] but it is not a readily available technology.

X-ray magnification can be applied to lower the resolution requirements of the detector. Two-dimensional x-ray magnification ($\times$20) was achieved for tomography by asymmetrical Bragg reflections from two Si crystals. A resolution of 1 μm was obtained in all three dimensions[4] at 8 keV. Mirrors under grazing incidence or Fresnel zone plates have been used with micrometer and submicrometer resolution.[5–7]

Luminescent screens in conjunction with electronic detectors offer on-line operation and a resolution that is principally limited by diffraction of (visible) light to approximately 0.3 μm. In terms of resolution, the crucial element is the luminescent screen. We demonstrate the feasibility of optically transparent, i.e., nonscattering, luminescent screens (scintillators) and their superiority in terms of spatial resolution versus detection efficiency, in particular compared with luminescent screens based on powder phosphors. Screens based on powder phosphors are commercially available down to a grain size of approximately 1 μm. Their resolution in terms of full width at half-maximum (fwhm) of the line spread function (LSF) is approximately equal to their thickness.[8] Homogeneous screens of 2–3-μm thickness and similar resolution can be deposited. A high-resolution detector based on a thin powder screen is described in Ref. 9. Smaller grain sizes have been manufactured, but in general with a loss in x-ray-to-light conversion efficiency.[10] The density of these powder screens is approximately half of that of the corresponding solid material, resulting in reduced absorption. Absorption of x rays with energies between 5 and 60 keV is generally low for the screen thickness, i.e., resolution, required. To overcome the resolution–thickness limitations, i.e., the proportionality between resolution and thickness, structured screens have been developed. They provide, to some extent, light guiding within the screen perpendicular to its surface.

0740-3232/98/071940-12$15.00

This can be achieved, e.g., by columnar growth of CsI:Tl (Ref. 11) or by some hollow masks filled with luminescent material. Based on the latter technology, a detector for microtomography at the National Synchrotron Light Source, Brookhaven National Laboratory, Upton, New York, has a resolution of 1 μm.[12,13] But this technology is not readily available, which led us to an approach based on optically transparent luminescent screens, also known as scintillators.

Detection systems employing transparent luminescent screens and lens optics differ from previously discussed systems in the following respect: the lens is focused into the transparent luminescent screen. The resolution therefore depends not only on the thickness of the screen but additionally on the depth of focus (or defect of focus) and the spherical aberration of the optics. Parallax between the incident x-ray beam and the optical axis may reduce resolution further. Scintillators have been used before for high-resolution imaging, but far above the diffraction limit and without considering the wave-front aberrations arising from defect of focus.[14,15] The ultimate limits of resolution are dictated by the diffraction limit of light—at least for imaging in the far field—and by the absorption processes of the x rays themselves. An x-ray photon deposits its energy in a finite volume through a process of electron propagation and fluorescent photon propagation. As shown in Subsection 2.A, this is not limiting the resolution in our case. The difficulties in producing small-grain-sized phosphors or small structured screens are replaced by the need to obtain thin layers of scintillators with a high atomic number (high Z) and optical quality surfaces. We present here a description of the image formation process and the physical limitations of the described detector setup for x-ray imaging. Its application can be easily extended to direct electron detection, e.g., in electron microscopy.

2. X-RAY IMAGING WITH TRANSPARENT LUMINESCENT SCREENS

To achieve high-resolution x-ray imaging, transparent luminescent screens (scintillators) are combined with diffraction-limited microscope objectives to magnify the x-ray image onto a CCD camera. The imaging system is depicted in Fig. 1(a). A low-divergence x-ray beam is partially absorbed by the luminescent screen and generates a visible-light image. The light image (object plane of the optical system) is relayed to the CCD (image plane). In our experiments the x-ray beam can be considered to be parallel, and it impinges perpendicularly onto the scintillator. Its divergence can also be neglected compared with the thickness and the resolution of the optical system. Therefore the light intensity distributions across arbitrary planes in the scintillator can be regarded as identical, apart from amplitude changes that are due to the attenuation of the x-ray beam. The influence of x-ray absorption processes on the imaging properties is neglected (see Subsection 2.A). These intensity distributions are imaged and summed up at the CCD. The CCD will be focused onto a specific object plane within the scintillator. The planes before and behind will be out of focus at the CCD but will nevertheless sum up to the total signal distribution. The image resolution is therefore determined by the amount of defect of focus of the image distributions before and behind the focal plane and, further, by diffraction and by spherical aberrations arising from the thickness of the scintillator and the substrate. Parallax by misalignment, i.e., an angle between x rays and optical axis, may also degrade the image quality.

The following parameters affect the spatial resolution R: the defect of focus δz (with respect to z_0), the numerical aperture NA = $n \sin \alpha$ of the optical relay system [Fig. 1(a)], the vacuum wavelength of light λ, and the substrate thickness t. The relations are given as

Defect of focus (Ref. 16, p. 101):

$$R \sim \delta z \mathrm{NA}, \tag{1a}$$

Diffraction (Ref. 17, p. 419):

$$R \sim \lambda/\mathrm{NA}, \tag{1b}$$

Spherical aberration (Appendix A):

$$R \sim t(\mathrm{NA})^3 \qquad (\text{if } t \gg \delta z). \tag{1c}$$

Hopkins[16] derived relation (1a) for a definite defect of focus. Relation (1a) is also valid in our case, i.e., the superposition of images with a different defect of focus. These relations will be analyzed in detail in Subsections 2.B and 2.C. First, the limitations on spatial resolution by the x-ray absorption process will be considered.

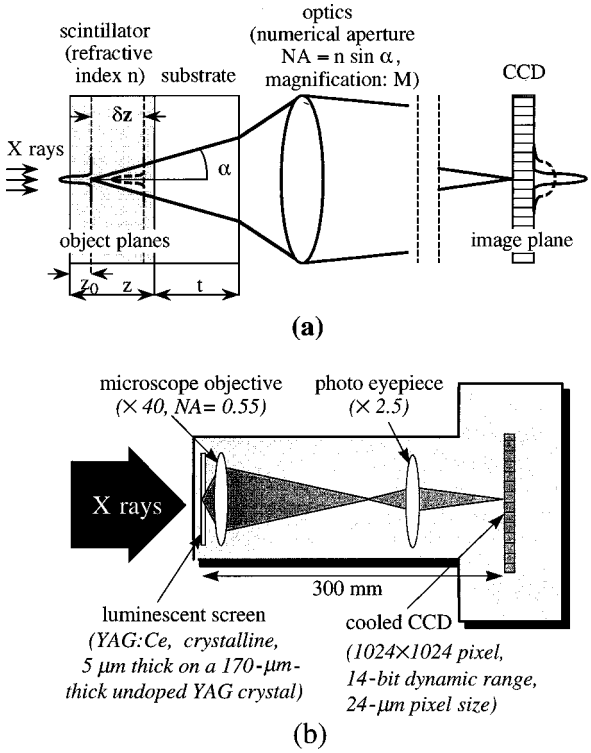

Fig. 1. (a) X-ray imaging with transparent luminescent screens (scintillators). Identical visible-light images are created by the x-ray beam in different planes of the scintillator. An image in plane z_0 is focused onto the CCD (solid curves). An image in plane $z_0 + \delta z$ is out of focus at the CCD (dashed curves). (b) Optical setup of the camera. The characteristics of the microscope objective determine the resolution. The photo eyepiece corrects for field curvature.

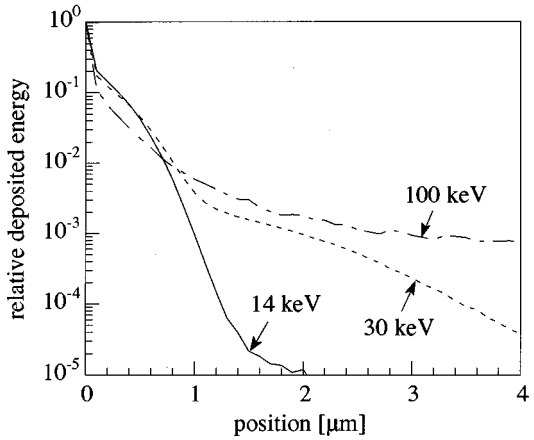

Fig. 2. Monte Carlo simulations of radial absorbed-dose distributions at x-ray energies of 14, 30, and 100 keV in a 5-μm-thick YAG:Ce scintillator on a 100-μm-thick undoped YAG substrate.

A. Absorbed-Dose Distribution in the Scintillator

The spatial resolution of imaging detectors may be limited by the spatial distribution of the deposited x-ray energy imparted from ionizing radiation. The limits arise since secondary processes, e.g., characteristic x rays and secondary electrons, may deposit energy far from the primary photon interaction site. The Integrated Tiger Series code for Monte Carlo simulation of photon and electron transport in matter[18,19] was used to derive radial absorbed-dose[20] distributions around a pencil beam of x rays impinging orthogonally onto a flat surface of a 100-μm-thick disk-shaped yttrium aluminum garnet (YAG) crystal with 5-mm diameter. A thickness of 100 μm is sufficient in the simulation to account for backscattered electrons and x rays. The energy deposition was sampled in a 5-μm-thick layer at the flat surface oriented toward the source and with a radial sampling distance of 100 nm. This thickness corresponds to that of the Ce-doped scintillating layer in the crystal used in the experiments described herein. The radial absorbed-dose distributions reflect the effects of the energy deposition on the point spread functions (PSF's) for the imaging system, i.e., effects that are due to ionizing radiation transport in the scintillator. Integrated Tiger Series simulations with the ACCEPTP code[18] were performed for monoenergetic photons in the range 5–100 keV. Both the electron-transport and the photon-transport cutoff energy was set to 1 keV. For particles with energies below this, the energy is considered to be locally absorbed. For each primary photon energy, radiation transport was simulated for 5×10^6 incident photons.

The results of the Monte Carlo simulations for 14-, 30-, and 100-keV incident photons are shown in Fig. 2. The dominant qualitative feature of the three curves is a very high relative absorbed dose in the central cylindrical scoring region around the pencil beam and a slower decrease with distance outside this cylinder. The reason for the very high absorbed dose in the center is that a considerable fraction of the energy deposition is by Auger electrons that have such low energies that, on the average, their continuous slowing down ranges are comparable with or smaller than the dimensions of the central (first) cylindrical energy scoring region. The energy deposited outside the first scoring region is caused by secondary electrons and characteristic x rays. If we consider only the radial energy deposition profile in the 5-μm-thick scintillating layer of the crystal, the fwhm indicates that the high-spatial-frequency response of our detector system is not limited by the crystal and is less than 100 nm. Since this is below the diffraction limit for any visible-light optical system, the three-dimensional energy deposition distribution in the 5-μm-thick YAG:Ce layer is not limiting the spatial resolution. On the other hand, it should be recognized that the tails of the radial energy distribution may have a deteriorating effect on the middle- and low-frequency parts of the modulation transfer function (MTF). It should also be pointed out that the high-energy density created by the short-range Auger electrons might affect the scintillation efficiency of the doped crystal, since it is known that for many materials the scintillation efficiency exhibits a dependence on the linear energy transfer of the charged particles that deposit energy in the detector.

B. Spatial Resolution Depending on Defect of Focus and Diffraction

The frequency response of an imaging system [optical transfer function (OTF)] suffering from defect of focus and diffraction has been derived by Hopkins[16] under the assumption of a circular aperture. We apply his formula to compute the resolution of our optical system.

As explained above, the image is found by superposing the intensity distributions originated in the different object planes. By the same argument, the LSF and its Fourier transform, the OTF of the system, are the sum of the individual response functions. Since the pupil function of the lens is symmetrical, the OTF is equal to its modulus, the MTF. The PSF is related to the LSF by an Abel transform.[21] The MTF of the imaging system can therefore be written as

$$\begin{aligned} \mathrm{MTF}(f) &= |\mathrm{OTF}(f)| \\ &= \left| \int_{-z_0}^{z-z_0} \mathrm{OTF}(f, \delta z) \exp[-\mu(\delta z + z_0)] \mathrm{d}\delta z \right|, \end{aligned} \tag{2}$$

where f denotes the spatial frequency in the object plane, z is the thickness of the scintillator, z_0 refers to the plane (the distance from the surface) where the optical system is focused at, and δz (with respect to z_0) is the defect of focus. The exponential term accounts for the absorption of x rays; μ is the absorption coefficient.

The MTF and the LSF have been calculated for different NA's and thicknesses z of the scintillator (examples are given in Subsection 4.B). The LSF curves significantly change their shape at large defect of focus and thickness z, i.e., pronounced tails appear. Therefore the fwhm is no longer an unambiguous criterion for the image quality. Instead, the spatial resolution R will now be expressed in terms of a full width, which covers 90% of the integrated LSF (fw90%int).

Figure 3 shows numerical simulations of Eq. (2) for $n = 1.95$, $\lambda = 550$ nm, and $z_0 = z/2 = \delta z_{\max}$. X-ray attenuation in the scintillator was not considered, i.e.,

$\mu = 0$. For low NA the optical system is diffraction limited, and defect of focus does not influence the performance of the system. For high NA the curves split up depending on the thickness of the scintillator, i.e., the amount of defect of focus.

Equation (3a) below is a fit to the plots of Fig. 3 that combines diffraction and defect of focus in one equation [cf. relations (1)]:

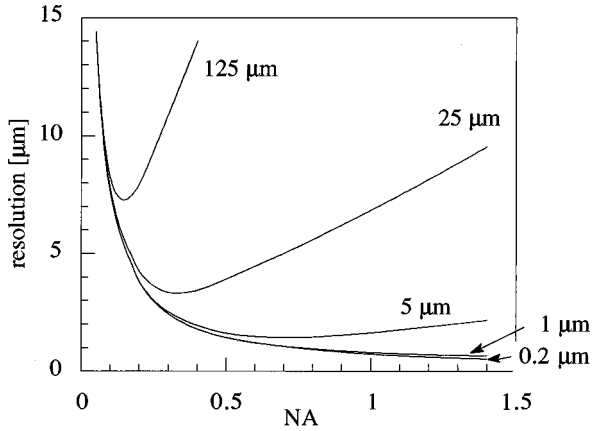

Fig. 3. Spatial resolution (R) versus numerical aperture (NA) of an optical system for different thicknesses (z) of a scintillator according to Eq. (2). The left wing is degraded by diffraction, the right one by defect of focus. Parameters used for computation are $n = 1.95$, $z_0 = z/2 = \delta z_{\max}$, and $\lambda = 550$ nm; R is in units of fw90% int.

$$R = \left[\left(\frac{p}{\mathrm{NA}}\right)^2 + (qz\mathrm{NA})^2\right]^{1/2}, \tag{3a}$$

$$p = \begin{cases} 0.70\ \mu\mathrm{m} & \text{at fw90\%int} \\ 0.18\ \mu\mathrm{m} & \text{at fw50\%int} \end{cases},$$

$$q = \begin{cases} 0.28 & \text{at fw90\%int} \\ 0.075 & \text{at fw50\%int} \end{cases}, \tag{3b}$$

where R and z are in micrometers. The coefficients p and q are given for the cases of 90% and 50% integrated LSF. The first term in Eq. (3a) is due to diffraction, and the second term is due to defect of focus. For a required resolution R, a specific curve $R_z(\mathrm{NA})$ exists that has its minimum at R, with parameters $\mathrm{NA}_{\mathrm{opt}}$ and z_{opt}. These parameters characterize the best optical design, i.e., lowest NA and highest z for a certain resolution R:

$$z_{\mathrm{opt}} = \frac{1}{2pq} R^2, \qquad \mathrm{NA}_{\mathrm{opt}} = \sqrt{2}p \frac{1}{R}. \tag{4}$$

The optical setup that so far gave the highest resolution (Table 1) employed an YAG:Ce screen with thickness $z = 5\ \mu$m and NA = 0.55. From Fig. 3 an improvement in resolution of a factor of 2 is expected for a system with $z = 1\ \mu$m and NA = 1.

Other definitions of resolution are often used: (1) the fwhm of the LSF and (2) the resolution of a microscope[17]

Table 1. Detector Characteristics

X-ray entrance window	Light-tight, aluminized polyester foil Foil thickness: 2 μm × 12 μm Supplier: Compagnie Franco Suisse, Illfurth, France
Scintillator	5-μm-thick YAG:Ce ($Y_3Al_5O_{12}$:Ce) (refractive index $n = 1.95$, central wavelength $\lambda = 550$ nm, energy conversion efficiency of luminescence $\eta_{x/v} = 0.07$, density of scintillator $\rho_{\mathrm{scint}} = 4.55$ g/cm^3) on a 170-μm-thick substrate of undoped YAG Supplier: Crismatec, Nemours, France Proposed scintillator: LSO:Ce (Lu_5SiO_5:Ce) ($n = 1.82$, $\lambda = 420$ nm, $\eta_{x/v} = 0.06$, $\rho_{\mathrm{scint}} = 7.4$ g/cm^3)
Optics	Objective LWD CD plan, magnification ×40, numerical aperture NA = 0.55 Photo eyepiece: NFK 2.5, magnification 2.5 Supplier: Olympus-Europe, Hamburg, Germany
CCD camera	Photometrics CH250 14-bit dynamic range, Peltier/water cooled, 1024^2 pixels, $(24\ \mu\mathrm{m})^2$ pixel size, readout time 5 s Quantum efficiency $\eta_{v/e} \approx 0.3$ at 550 nm Manufacturer: Photometrics, Tucson, Ariz.
Sensitive area	$\approx(0.3\ \mathrm{mm})^2$ with pixel size $(0.3\ \mu\mathrm{m})^2$ referred to input
Spatial resolution	Calculated from data with boron fiber (Subsection 4.B): modulation transfer function: 280 lp/mm at 50%; which corresponds to line spread function (LSF): 0.8 μm fwhm Directly measured with slit and corrected for slit width (Subsection 4.A): LSF: 1.1 μm fwhm
Detective quantum efficiency (DQE)	≈3% calculated, limited by absorption of x rays in the scintillator

(first zero of the Bessel function, or Airy disk). If the optical system is diffraction limited, these definitions are related to each other by

$$R_{\text{fw90\%int}} = 2.6R_{\text{fwhmLSF}} = 2.1R_{\text{microscope}}. \tag{5}$$

Resolution is approximately limited to $R = R_{\text{fw90\%int}} = 0.5\ \mu\text{m}$ (or $R_{\text{fwhmLSF}} = 0.2\ \mu\text{m}$) for $\lambda = 550$ nm, $n = 1.95$, and NA ≈ 1.4. A NA of 1.4 is achieved with objectives using immersion liquids. Using scintillators that emit light at a shorter wavelength would also improve resolution.

C. Spatial Resolution Depending on Spherical Aberrations

The foregoing considerations assume an optical system that is corrected for spherical aberrations arising from the thickness of the scintillator or from the substrate. However, the manual compensation for thick glass substrates provided by some commercial microscope objectives usually do not correct for the high refractive index ($n \approx 2$) of the scintillators of interest used here (YAG, $n = 1.95$). Instead, they correct for ordinary glass ($n' = 1.5$).

Born and Wolf (Ref. 17, p. 472) derived a tolerance condition for spherical aberrations that implies that the maximum deviation of the wave front be less than 0.94 of a wavelength. If the Seidel coefficient for a plane-parallel plate is introduced (see Appendix A), this tolerance condition is given by

$$\frac{1}{2}\,(\text{NA})^4 t\,\frac{n^2-1}{2n^3} < 0.94\lambda. \tag{6}$$

The maximum thickness t of a plate (here the thickness of the scintillator and its substrate) that satisfies relation (6) is calculated for different optical systems: (1) without any correction for spherical aberrations [relation (7a) below]; (2) with correction for a certain plate thickness but at a refractive index n' different from that of the scintillator [relation (7b)]; and (3) if the microscope objective allows a spherical aberration correction, then the deviation from the required refractive index can be compensated by a slightly different choice of thickness t' [Eq. (7c)]. For the calculations, $n = 1.95$, $n' = 1.5$, and $\lambda = 550$ nm were used:

$$t_a < 0.94\lambda\,\frac{2}{(\text{NA})^4}\,\frac{2n^3}{n^2-1},$$

$$t_a < 60\ \mu\text{m}\ (\text{NA} = 0.55),\quad t_a < 6\ \mu\text{m}\ (\text{NA} = 1), \tag{7a}$$

$$t_b < 0.94\lambda\,\frac{2}{(\text{NA})^4}\left(\frac{2n^3}{n^2-1} - \frac{2n'^3}{n'^2-1}\right),$$

$$t_b < 3\ \text{mm}\ (\text{NA} = 0.55),\quad t_b < 300\ \mu\text{m}\ (\text{NA} = 1), \tag{7b}$$

$$t' = \frac{n^2-1}{n^3}\,\frac{n'^3}{n'^2-1}\,t,$$

$$t' = 1.02t. \tag{7c}$$

Hence, for the realized system (specifications given in Table 1), correction for spherical aberration is required [relation (7a)]. The commercial microscope objective provides a correction at $n = 1.5$, which is sufficient for $t = 170\ \mu$m [relation (7b)]. A system with NA = 1 requires a more careful correction [relation (7b)].

D. Detective Quantum Efficiency

So far we have concentrated on the problem of spatial resolution and its characterization. It was the primary goal to achieve the highest possible spatial resolution. Other characteristics have been compromised in favor of resolution. Here some guidelines are given to show to what extent an increase in spatial resolution of the detector degrades the signal-to-noise ratio (SNR). Three designs are considered (data in Table 2): (a) the existing detector, (b) a design with a 1-μm-thick YAG:Ce scintillator (NA = 1), and (c) a design like (b) but with a higher-Z scintillator. Design (b) is expected to improve the resolution by a factor of 2 (Subsection 2.B), and (c) would enhance the absorption with respect to (b).

Considering the detector response only at low spatial frequencies and in shot-noise-limited operation, we define detective quantum efficiency (DQE) as[22–24]

$$\text{DQE} = \frac{\text{SNR}_{\text{out}}^2}{\text{SNR}_{\text{in}}^2} \approx \eta_{\text{abs}}\left(1 + \frac{1 + 1/\eta_{v/e}}{\eta_{\text{col}}(E_x/E_v)\,\eta_{x/v}}\right)^{-1}$$

$$\xrightarrow[\text{camera})]{\text{(realized}} \eta_{\text{abs}} \propto \frac{Z^4}{{E_x}^3}\,\rho_{\text{scint}}, \tag{8}$$

where SNR_{in} and SNR_{out} are the SNR's at the input and the output of the detector, $\eta_{\text{abs}}(E_x, Z, z)$ denotes the absorption efficiency for x rays by the luminescent screen, E_x is the x-ray energy, Z is the effective atomic number of the scintillator, z is its thickness, $\eta_{x/v}$ is the energy conversion efficiency of x rays to visible light, E_v is the photon energy of the visible-light photons, $\eta_{\text{col}}(\text{NA}) \approx \frac{1}{4}(\text{NA}/n)^2$ is the collection efficiency of light from a transparent luminescent screen collected by an optical system, $\eta_{v/e}(\lambda)$ is the quantum efficiency of the CCD, and

Table 2. DQE for Three Detector Designs, Calculated According to Eq. (8) with Computational Parameters from Table 1

Detector Design	Resolution (fw90%int) (μm) [Eq. (3a)]	X-Ray Energy (keV)	Absorption Efficiency	DQE [Eq. (8)]
Existing				
5-μm YAG:Ce	1.5	14	0.04	0.026
NA = 0.55		30	0.04	0.032
Design				
1-μm YAG:Ce	0.8	14	0.008	0.0069
NA = 1		30	0.006	0.0056
1-μm LSO:Ce	0.8	14	0.08	0.066
NA = 1		30	0.01	0.0091

ρ_{scint} is the density of the scintillator. Hence DQE $= \eta_{\text{abs}}$ in the case of sufficiently high conversion and collection efficiency.

For the three systems (a)–(c), the DQE is computed and given in Table 2. The expected spatial resolution according to Eq. (3a) is given for comparison. DQE is mainly determined by absorption in all three cases. It is noteworthy that a luminescent screen based on powder phosphors could have a thickness of only approximately 1–2 μm to achieve the same spatial resolution[8]; i.e., absorption and DQE would be lower. The absorption of a powder phosphor screen is further reduced, approximately by a factor of 2, by the packing density of the powder grains. For applications considering a 1-μm-thick scintillator, especially at high energies, a high Z and a dense scintillator such as cerium-doped lutetium oxyorthosilicate (LSO:Ce) are beneficial.

Conversion efficiency $\eta_{x/v}$ slightly degrades DQE in the above examples (Table 2). If the conversion efficiency is larger than that given in condition (9) below, DQE is not degraded [cf. relation (8)]. A value for the conversion efficiency above this threshold does not improve DQE:

$$\eta_{x/v} > \frac{1+\dfrac{1}{\eta_{v/e}}}{\eta_{\text{col}}\dfrac{E_x}{E_v}} = \begin{cases} \text{system (a)} & 4\% \text{ at } 14 \text{ keV} \\ \text{system (b)} & 0.9\% \text{ at } 14 \text{ keV}. \\ \text{system (c)} & 1\% \text{ at } 14 \text{ keV} \end{cases} \tag{9}$$

3. DETECTOR DESIGN AND CHARACTERISTICS

The setup is schematically shown in Fig. 1(b). A microscope objective magnifies the object plane by a factor of 40 at a finite distance (tube length 160 mm). The objective has a built-in correction for glass cover slips. A photo eyepiece corrects for the remaining field curvature and magnifies the object plane further. The components of the detector are listed in Table 1, together with their performance specifications.

4. MEASURING MICROMETER SPATIAL RESOLUTION

An important issue is to establish a precise technique to measure the spatial resolution of hard-x-ray detectors in the micrometer and submicrometer range. In visible and soft-x-ray optics, detectors are most often characterized by measuring the PSF or the LSF of the system. We describe two methods. The first is the measurement of the detector response to the x-ray exposure of a slit [Fig. 4(a)]. The second is a holography method to obtain the MTF directly [Fig. 4(b)]. Another appealing technique is to use the statistical properties of a uniform x-ray exposure. Pixel-to-pixel correlations yield the LSF.[25] Here the small detector gain prevents us from using this technique.

A. Measuring the Line Spread Function

For a direct measurement of the LSF, we collimated the beam of a laboratory x-ray generator by two tungsten slits to 1.2 μm [Fig. 4(a)]. Despite the lower number of photons emitted by the x-ray generator compared with that from a synchrotron source, we could realize LSF measurement within exposure times of typically 100 s. These exposure times were achieved with the broadband emission of a tungsten anode tube operated at 40 kV. The slit had been oriented parallel to the rows of the CCD, so that on-chip binning of pixels of the CCD in one direction reduced exposure times without degrading the spatial resolution. Tests at an x-ray generator are an interesting complementary method to measurements at a synchrotron source. This is due to practical advantages such as faster access to the facility and faster modifications of measurement conditions. Alternative methods to measure the LSF or the PSF with synchrotron radiation and focusing optics are summarized in Ref. 26.

The second slit in Fig. 4(a) defines the cross section of the x-ray beam that probes the detector response. It has a width of 1.2 μm and a thickness of 1 mm and consists of two polished tungsten (W) blades. The blades are joined together but separated by a 1.2-μm Al layer that was

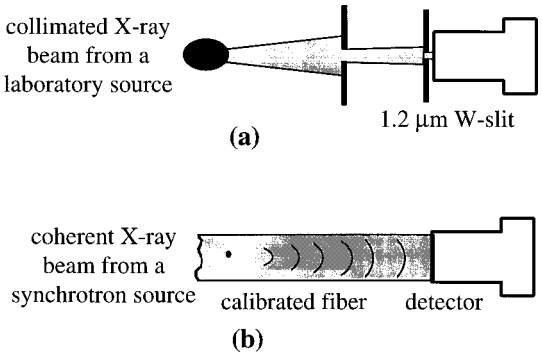

Fig. 4. Principle of the resolution measurement. (a) With an x-ray generator: to measure the line spread function (LSF) of the detector directly, the x-ray beam is collimated to 1.2 μm. The 1.2-μm slit is positioned in contact with the scintillator of the camera. The measured detector response is corrected for the slit width (W-slit) to obtain the LSF. (b) With synchrotron radiation: a wideband interference pattern is created for the direct measurement of the modulation transfer function (MTF) of the detector system. The fringe pattern is produced by interference of the unscattered plane wave with the scattered wave of a calibrated fiber. The spatial-frequency spectrum of the recorded pattern is normalized to the theoretically calculated interferogram to obtain the MTF.

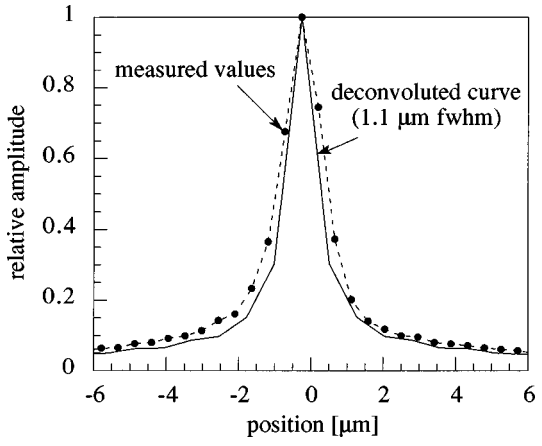

Fig. 5. Measurement of the detector response to x rays from a 1.2-μm slit. The LSF is calculated by deconvolving the measured values by the slit widths.

evaporated onto one of these blades at its borders. The slit is in close contact with the scintillator to prevent broadening of the x-ray beam behind the slit from total reflections and diffraction.

Figure 5 shows the cross section through the detector response of the slit measurement. For this measurement a photo eyepiece with a slightly different magnification ($\times 1.7$) was used. The measured curve is deconvolved by the slit width, which results in 1.1 μm fwhm. The parameters of the optical system are NA = 0.55 and a 5-μm-thick YAG:Ce scintillator. Figure 3 shows that such a system operates close to the diffraction limit, with a resolution of 1.5 μm fw90%int. Hence Eq. (5) can be applied; that is, a resolution of 0.6 μm fwhm is expected. Possible reasons for the deviation from theory are discussed in Section 6.

B. Measuring the Modulation Transfer Function

In principle, the MTF can be calculated analytically from the LSF or the PSF of the system if these functions are known exactly enough over a large spatial area. However, it is often more convenient and appropriate to measure the MTF of the detector directly. We measure the MTF of the detector system by analyzing the recording of an interference pattern. Such a pattern can be produced by taking holographic images of weakly scattering objects in the coherent beam of a third-generation synchrotron source.[27] It produces a broadband diffraction pattern that gives direct rise to the frequency response of the optical system. This technique has two advantages over direct LSF/PSF measurements: (1) easier alignment that is due to a very large depth of field of the diffraction pattern and (2) holographic images with sufficient SNR at x-ray photon energies as high as 60 keV. The intensity distribution of a coherent x-ray beam after transmission through such weakly scattering objects can be described in the framework of Fresnel diffraction[27] and is characterized by strong oscillations in intensity at boundaries and interfaces in the object. The coherence condition is satisfied by monochromatizing the beam and by the given geometrical setup at a European Synchrotron Radiation Facility (ESRF) beamline, i.e., a small source size (30-μm fwhm vertical source size) and a large source-to-sample distance (40 m). The spacing between two oscillations becomes smaller as the distance to the interface is made larger. The smallest fringe spacing is given by the source size and the demagnification factor, i.e., the ratio of the source-to-sample distance to the sample-to-detector distance. In our case the smallest fringes (and thus the highest spatial frequencies in the detector plane) are spaced approximately 0.1 μm apart. We used a 100-μm-thick boron (B) fiber with a 15-μm-diameter W core as a reference object. Figure 6 shows a cross section through the interferogram. To obtain the MTF of the detector, the measured frequency spectrum of the recorded holograms is normalized to the theoretical frequency spectrum in the detector plane.

Measurements were taken at 12 keV and at a distance of 22 cm between the B fiber and the detector. Figure 7 shows the results for the 5-μm-thick YAG crystal. The simulated curve was convolved with the pixel size given by the CCD to correct for the reduction of the MTF by

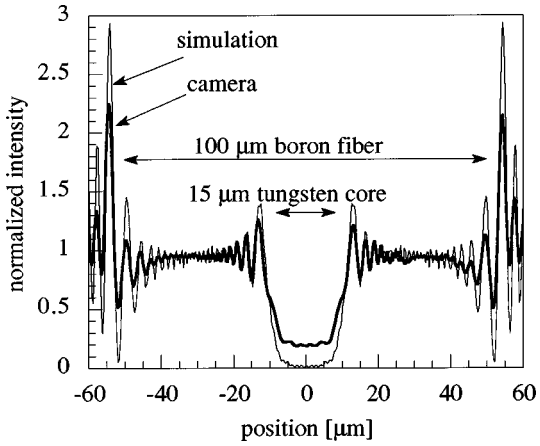

Fig. 6. Cross section through the holographic image of a boron (B) fiber cross with a 15-μm-thick tungsten (W) core. The absorption of the W core is clearly visible (center). Fringe spacing is decreasing for increasing distance from the edge. The cross sections were taken over the B edge to measure directly the MTF of the detector.

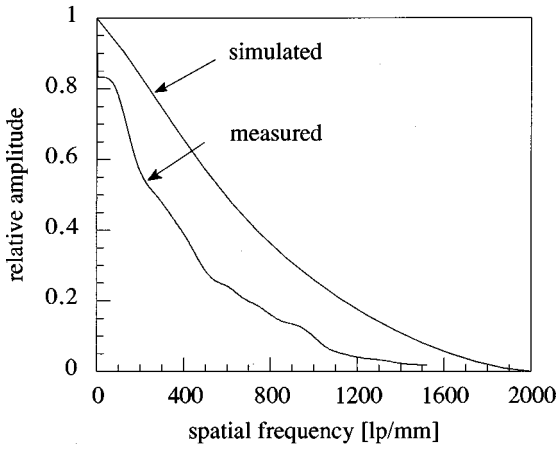

Fig. 7. MTF's for the detector with a 5-μm-thick YAG scintillator and an optical system with NA = 0.55. The simulated curve was convolved with the pixel size defined by the CCD camera.

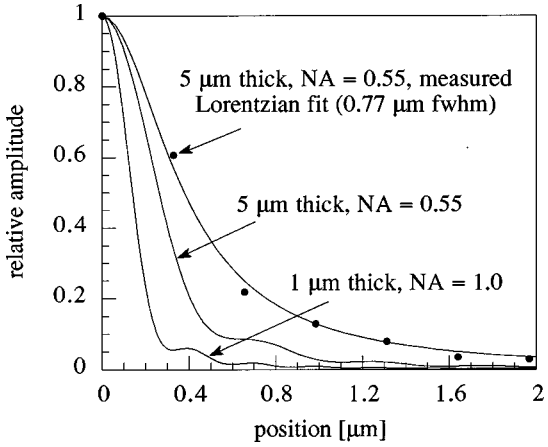

Fig. 8. LSF's for x-ray imaging with scintillators of different thicknesses (5 and 1 μm) and different NA's. The measured values are fitted with a Lorentzian curve.

sampling. The measured frequency response is 1000 lp/mm at 10%. The low-frequency drop indicates pronounced tails in the LSF. We assume that internal re-

flections in the scintillator, which are eventually coupled out at inhomogeneities, are responsible for this. A further discussion is given in Section 6.

The LSF's (Fig. 8) were obtained by Fourier-transforming the MTF curves. The LSF is shown for the actual existing system, the simulation of this system, and the already proposed optimized design from Subsection 2.D (NA = 1, 1-μm-thick scintillator). A LSF of 0.8 μm fwhm is calculated for the measured data, which is better than that for the slit measurement in Subsection 4.A. The simulated LSF provides 0.6 μm fwhm [or 1.5 μm fw90%int (Fig. 3)]. The deviation of the experimental value from the calculated one is discussed in Section 6. The curve for an optical design (NA = 1, 1-μm-thick scintillator), which is optimized for highest resolution, is added to demonstrate the resolution limits of this imaging technology. In this case 0.3 μm fwhm of the LSF is achievable. On the other hand, this gain in resolution can be achieved only by a strongly reduced thickness of the scintillator. Hence resolution is balanced against absorption of x rays and DQE (see Subsection 2.D).

5. APPLICATIONS

The high-resolution camera as described above has been used for approximately one year at bending-magnet and undulator beamlines at the ESRF. Even after several hundred hours of exposure in x-ray beams with intensities of up to 10^{13} photons s^{-1} mm^{-2}, degradation that is due to radiation damage is not visible. The camera has been used in routine beamline commissioning applications as a beam-position monitor in order to measure the spot sizes of focusing x-ray optics, but mainly to obtain projection images and tomograms in absorption and phase contrast mode.[28,29] Phase contrast imaging gives additional contrast at edges and interfaces in a sample as a result of the phase shift of a coherent x-ray beam inside the sample. This gives the opportunity to image low-absorption objects such as organic or low-Z materials with sufficient contrast at room temperature and under normal pressure conditions. Imaging of wet samples, which is an important issue in medical and biological applications, is also possible.

The experimental setup for phase contrast imaging is identical to the in-line holography setup for the direct MTF measurement shown in Fig. 4(b). The object-to-detector distance is 5–100 cm, and the x-ray energy is between 15 and 60 keV, depending on the size and the composition of the sample features of interest. Figure 9 shows the projection image of a Foraminifera shell in phase contrast mode at 25-cm distance in a 25-keV beam. The image is flat-field corrected to eliminate beam-related artifacts, which are due to imperfections in the optical el-

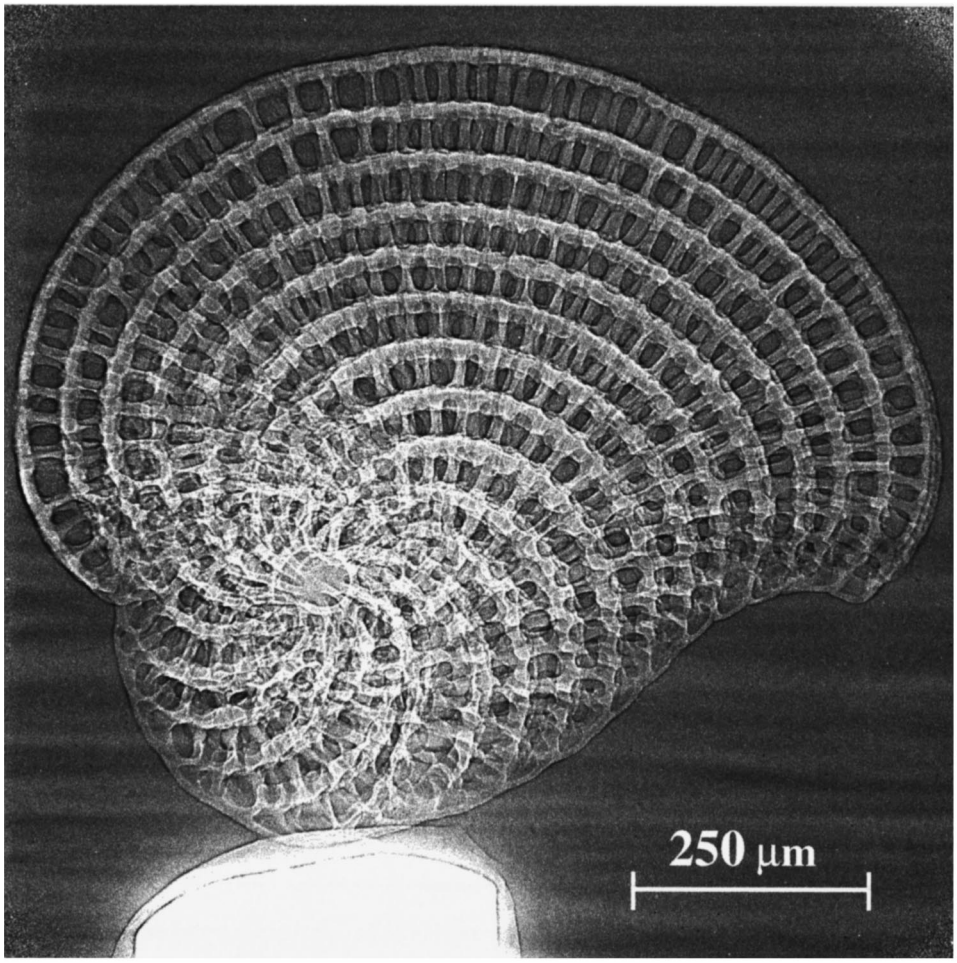

Fig. 9. Imaging of a Foraminifera shell at 25 keV in phase contrast (distance to the detector: 10 cm).

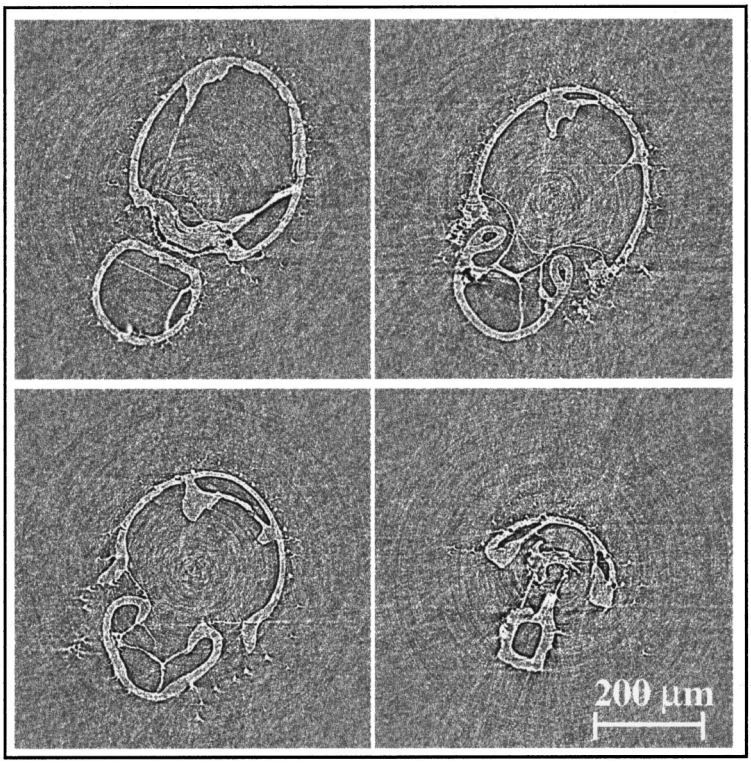

Fig. 10. Four tomographic reconstructed cross sections through an insect's knee (crane fly). For the tomogram 500 phase contrast images were recorded at 20 keV. Details of sizes down to 2 μm, such as tendons, are clearly visible.

ements and windows in the x-ray beam.[30] The edge-enhancing effect in phase contrast mode is clearly seen at the chamber divisions. The field of view is 600 μm $\times$ 600 μm, and the exposure time at a bending-magnet beamline was 20 s.

Phase contrast imaging can easily be combined with computed tomography to give three-dimensional information about an object. For this a set of images of different angles of view of the object has to be taken. For the reconstructed cross sections of a knee of an insect (Fig. 10), 500 phase contrast images were taken over an angular range of 180°. The total recording time (including the time to save the images to disks) was approximately three hours. The projections were processed by a standard tomographic filtered backprojection algorithm.

Further applications for such a detector system are seen in high-energy x-ray holography, topography, and time-resolved imaging. These techniques seem to have promising applications in, for example, the study of liquid–air interfaces, which are of fundamental importance in soil science. This detector system should prove useful in various applications in materials science, medicine, and biology, where two- and three-dimensional information or time-resolved measurements are sought at 1-μm spatial resolution.

6. DISCUSSION

The spatial resolution of the detector is characterized in two ways. One method measures the detector response to a wide spatial-frequency spectrum (B fiber), and the other method measures the response to a slit. From both measurements the LSF curves are calculated and found to be in close agreement with each other, that is, 0.8 μm fwhm for the B fiber and 1.1 μm fwhm for the slit. What may be responsible for the difference in these results are some parameters of the experimental conditions that have been difficult to control. These parameters are the slit-to-scintillator distance, the slit profile, mechanical instabilities, and electrical interference. The geometrical slit profile is well known, but its transmission profile under x-ray exposure is not. A rectangular function is assumed; however, the edges of the slit are partially transparent to x rays. We reduced the influence on the image quality by vibrations from the flow of cooling water through the CCD camera and by electrical pickup from the power supplies of stepper motors. The deviations between our measurements and the theoretical predictions (0.6 μm fwhm of the LSF) may also be due to these reasons. The remaining spherical aberrations by the substrate of the scintillator are a further potential cause for loss in resolution. We reduced the demand on the precision of alignment by thinning the substrate of our scintillator from 1 mm to 170 μm. A thinner scintillator requires a less precise compensation for spherical aberrations.

The total internal reflected light is another issue of concern. The light trapped in the scintillator represents 86% ($n = 2$) of the total amount of light produced. Ideally, it escapes to the end walls. The surface of the scintillator that was used, however, is not polished. Even though it was grown onto a polished substrate, surface inhomogeneities are visible. These inhomogeneities may couple total internal reflected light out, so that it contrib-

utes to tails in the LSF. The drop of the measured MTF at low spatial frequencies (Fig. 7) may have its cause in this effect. A reduction of tails has been reported for applications of scintillators in cathode-ray tubes. A thin (0.25-μm), index-matched, and light-absorbing layer was deposited onto the scintillator. This layer had to be sufficiently thin to be transparent for electron beams in this application.[31] Antireflection coatings have been used to improve light collection efficiency and resolution. The use of immersion liquids between objective and scintillator will also reduce the total internal reflected light.

Tails in the LSF or the PSF also occur as a result of the absorption processes in the scintillator at high x-ray energies as discussed in Subsection 2.A. In Fig. 11 energy deposition profiles at different energies can be compared with the PSF of our optical system. The PSF's have been calculated from the LSF's in Fig. 8 by using the Abel transform. The PSF of our detector, measured at 12 keV, is not limited by the energy deposition. For energies greater than 30 keV, the theoretical PSF starts to overlap with the energy deposition profile. This indicates that the resolution of our detector is nearly limited by absorption, at least at low spatial frequencies.

Other parameters remain to be studied. Radiation damage is one of them. Reflecting-light optics are being considered to avoid darkening of the lenses by x rays. Exposure time is another important parameter. High intensities or long exposure times are required for high spatial resolution, since a certain SNR has to be provided per pixel. Exposure time is of prime importance, especially in microtomography, where several hundred images for each tomogram have to be taken to fulfill the sampling theorem.[32] Typically, exposure times are of the order of 10 s for the present detector at ESRF undulator beamlines (10^{13} photons $s^{-1}\,mm^{-2}$ in a monochromatic beam with a relative bandwidth of 10^{-4}). An increase in x-ray absorption of the scintillator, i.e., DQE of the detector (cf. Table 2), would reduce exposure times accordingly.

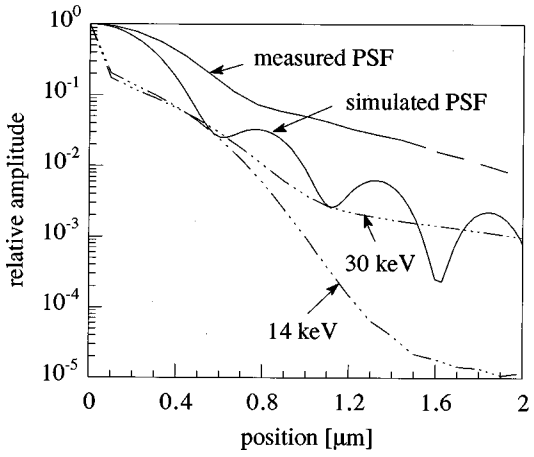

Fig. 11. Point spread functions (PSF's) of the optical system and profiles for the energy deposition in the scintillator. The measured and simulated PSF's are calculated from the LSF's of Fig. 8, and the energy deposition profiles are curves from Fig. 2. The parameters of the optical system for both measured and simulated PSF's are NA = 0.55 and a 5-μm-thick scintillator.

7. CONCLUSIONS

X-ray imaging with transparent luminescent screens has been shown to be a successful approach in obtaining submicrometer resolution. The image formation process has been described theoretically. Numerical simulations allow the prediction of the resolution of different optical systems as a function of their NA and the thickness of the scintillator. By exploiting the coherence of the synchrotron beam, we have established a convenient method for testing the spatial resolution.

The present system is close to its theoretical performance in terms of spatial resolution. A possible improvement in resolution by a factor of 2 down to 0.3 μm fwhm of the LSF is predicted by theory. Using scintillators at shorter wavelengths will further enhance resolution. However, an increase in resolution requires a reduction in thickness of the scintillator and hence a reduction in absorption and DQE. The relations between these parameters are given in this paper, and they allow one to optimize a detector system to its specific needs. Beyond approximately 0.3 μm, different detector technologies have to be considered that are not based on x-ray-to-light conversion. But for the desired spatial resolution in the range 0.7–2 μm, the combination of transparent luminescent screens with optical magnification appears to be a good compromise among technical feasibility, DQE, price, and resistance to radiation damage.

APPENDIX A: SPHERICAL ABERRATION OF AN IMAGING SYSTEM BY A PLANE-PARALLEL PLATE

A plane-parallel plate with refractive index n in air, situated between exit pupil and image plane of an optical system, introduces an angle-dependent (β) shift of focus Δz (Ref. 33, p. 310):

$$\Delta z(\rho) \approx t\,\frac{n-1}{n} + t\,\frac{n^2-1}{2n^3}\sin^2\beta(\rho)$$

$$\text{with}\quad \tan\beta(\rho) = \frac{a\rho}{r}, \tag{A1}$$

where t is the thickness of the plate, ρ is the normalized radial position of the rays in the exit pupil, a is the radius of the exit pupil, and r is the distance from exit pupil to image of the imaging system. This shift of focus Δz in the image plane is formally equivalent to a wave aberration or phase shift $\Phi(\rho)$ in the plane of the exit pupil of the following form (Ref. 17, p. 462):

$$\Phi(\rho) = \frac{1}{2}\left(\frac{a}{r}\right)^2 \Delta z\rho^2 \qquad \text{with}\quad \frac{a}{r} = \sin\alpha' = \text{NA}. \tag{A2}$$

The angle α' refers to the angle outside the plate. Introducing relation (A1) into Eq. (A2) and assuming that $\sin\beta \approx \tan\beta \approx \beta$ give

$$\Phi(\rho) = \frac{1}{2}(\mathrm{NA})^2 t \frac{n-1}{n}\rho^2 + A\rho^4$$

$$\text{with } A = \frac{1}{2}(\mathrm{NA})^4 t \frac{n^2-1}{2n^3}. \qquad \text{(A3)}$$

The second term of this wave aberration function characterizes spherical aberrations. The coefficient A is the Seidel coefficient for primary spherical aberration for a plane-parallel plate. Equation (A3) is the phase deviation of the pupil function of the optical system. The autocorrelation function of the pupil function is the frequency response function (OTF). Black and Linfoot[34] calculated the OTF for primary spherical aberrations.

Introducing the Seidel coefficient A [Eq. (A3)] into the formula for the lateral displacement of rays by spherical aberration given by Born and Wolf (Ref. 17, p. 471) reveals the relation for the resolution R (cf. ray-tracing analysis[35]):

$$R \propto t \frac{n^2-1}{2n^3}(\mathrm{NA})^3. \qquad \text{(A4)}$$

ACKNOWLEDGMENTS

We thank C. Ferrero of the European Synchrotron Radiation Facility (ESRF) for the implementation of the Abel transform routine, which was used to calculate the point spread function, A. Schröter of Olympus for his advice on microscope objectives, the members of the microfluorescence, imaging and diffraction (μ-FID) beamline at the ESRF for their support during the experiments, and M. Pecheux (Nice, France) for the Foraminifera samples.

REFERENCES

1. S. Lindaas, M. Howells, C. Jacobsen, and A. Kalinovsky, "X-ray holographic microscopy by means of photoresist recording and atomic-force microscopic readout," J. Opt. Soc. Am. A **13**, 1788–1800 (1996).
2. K. Kinoshita, T. Matsumura, Y. Inagaki, N. Hirai, M. Sugiyama, H. Kihara, N. Watanabe, Y. Shimanuki, and A. Yagashita, in *X-Ray Microscopy III*, Vol. 67 of Springer Series in Optical Sciences, A. Michette, G. Morrison, and C. Buckley, eds. (Springer-Verlag, Berlin, 1992), pp. 335–337.
3. Y. Okamoto, T. Oguro, I. Kashima, D. Kanishi, T. Sakurai, and T. Matsuki, "Development of the computed electroradiography: trial manufacture of digital imaging system," Radiology **185**, 395 (1992).
4. M. D. Silver, "Towards a micrometer resolution x-ray tomographic microscope," in *X-Ray Microbeam Technology and Applications*, W. Yun, ed., Proc. SPIE **2516**, 135–147 (1995).
5. R. Kodama, N. Ikeda, Y. Kato, Y. Katori, T. Iwai, and K. Takeshi, "Development of an advanced Kirkpatrick–Baez microscope," Opt. Lett. **21**, 1321–1323 (1996).
6. B. Lai, W. Yun, Y. Xiao, L. Yag, D. Legnini, Z. Cai, A. Krasnoperova, F. Cerrina, E. DiFabrizio, L. Grella, and M. Gentili, "Development of a hard x-ray microscope," Rev. Sci. Instrum. **66**, 2287–2289 (1995).
7. W. S. Haddad, I. McNulty, J. E. Trebes, E. H. Anderson, R. A. Levesque, and L. Yang, "Ultrahigh-resolution x-ray topography," Science **266**, 1213–1215 (1994).
8. R. K. Swank, "Calculation of modulation transfer functions of x-ray fluorescent screens," Appl. Opt. **12**, 1865–1870 (1973).
9. A. Koch and C. Riekel, "X-ray video camera with 10 μm spatial resolution," Rev. Sci. Instrum. **67**, 1737–1740 (1996).
10. H. B. Beverloo, A. van Schadewijk, J. Bonnet, R. van der Geest, R. Runia, N. P. Verwoerd, J. Vrolijk, J. S. Ploem, and H. J. Tanke, "Preparation and microscopic visualization of multicolor luminescent immunophosphors," Cytometry **13**, 561–570 (1992).
11. K. Oba, M. Ito, M. Yamaguchi, and M. Tanaka, "A CsI(Na) scintillation plate with high spatial resolution," Adv. Electron. Electron Phys. **74**, 247–255 (1988).
12. B. P. Flannery, H. W. Deckman, W. G. Roberge, and K. L. d'Amico, "Three dimensional x-ray microtomography," Science **237**, 1439–1444 (1987).
13. H. W. Deckman, J. H. Dunsmuir, and S. M. Gruner, "Microfabrication of cellular phosphors," J. Vac. Sci. Technol. B **7**, 1832–1835 (1989).
14. U. Bonse, R. Nusshardt, F. Busch, R. Pahl, J. H. Kinney, Q. C. Johnson, R. A. Saroyan, and M. C. Nichols, "X-ray tomographic microscopy of fibre-reinforced materials," J. Mater. Sci. **26**, 4076–4085 (1991).
15. F. Busch, "Auflösungsvermögen einer Mikrotomographie-Kamera für Röntgen-Synchrotronstrahlung," Ph.D. dissertation (University of Dortmund, Dortmund, Germany, 1994).
16. H. H. Hopkins, "The frequency response of a defocused optical system," Proc. R. Soc. London, Ser. A **231**, 91–103 (1955).
17. M. Born and E. Wolf, *Principle of Optics*, 6th ed. (Pergamon, Oxford, 1986).
18. J. L. Halbleib, R. F. Kensek, T. A. Mehlhorn, G. D. Valdez, S. M. Seltzer, and M. J. Berger, "ITS version 3.0: the integrated TIGER series of coupled electron/photon Monte Carlo transport codes," Rep. SAND91-1634 (Sandia National Laboratories, Albuquerque, N.M., 1988).
19. J. L. Halbleib, "Structure and operation of the ITS code system," in *Monte Carlo Transport of Electrons and Photons*, T. M. Jenkins, W. R. Nelson, and A. Rindi, eds. (Plenum, New York, 1987), pp. 249–262.
20. International Commission on Radiation Units and Measurements (ICRU), "Radiation quantities and units," Rep. 33 (ICRU, Washington, D.C., 1980).
21. J. C. Dainty and R. Shaw, eds. *Image Science*, 5th ed. (Academic, London, 1992).
22. U. W. Arndt and D. J. Gilmore, "X-ray television area detectors for macromolecular structural studies with synchrotron radiation sources," J. Appl. Crystallogr. **12**, 1–9 (1979).
23. A. Koch, M. Hagelstein, A. San Miguel, A. Fontaine, and T. Ressler, "Scintillating screen-CCD camera using analog on chip storage for time-resolved x-ray absorption spectroscopy," in *Cameras and Systems for Electronic Photography and Scientific Imaging*, C. N. Anagnostopoulos and M. P. Lesser, eds., Proc. SPIE **2416**, 85–93 (1995).
24. E. Breitenberger, "Scintillation spectrometer statistics," in *Progress in Nuclear Physics*, O. R. Frisch, ed. (Pergamon, New York, 1955), Vol. 4, pp. 56–94.
25. E. Dufresne, R. Brüning, M. Sutton, B. Rodricks, and G. B. Stephenson, "A statistical technique for characterizing x-ray position-sensitive detectors," Nucl. Instrum. Methods Phys. Res. A **364**, 380–393 (1995).
26. A. Snigirev, "The recent development of Bragg–Fresnel crystal optics: experiments and applications at the ESRF," Rev. Sci. Instrum. **66**, 2053–2058 (1995).
27. A. Snigirev, I. Snigireva, V. Kohn, S. Kuznetsov, and I. Schelokov, "On the possibilities of x-ray phase contrast microimaging by coherent high-energy synchrotron radiation," Rev. Sci. Instrum. **66**, 5486–5492 (1995).
28. C. Raven, A. Snigirev, I. Snigireva, P. Spanne, A. Souvorov, and V. Kohn, "Phase-contrast microtomography with coherent high-energy synchrotron x-rays," Appl. Phys. Lett. **69**, 1826–1828 (1996).
29. P. Cloetens, R. Barrett, J. Baruchel, J. Guigney, and M. Schlenker, "Phase objects in synchrotron radiation hard x-ray imaging," J. Phys. D **29**, 133–146 (1996).
30. A. Snigirev, I. Snigireva, V. Kohn, and S. Kuznetzov, "On the requirements to the instrumentation for the new generation of the synchrotron radiation sources: beryllium

windows," Nucl. Instrum. Methods Phys. Res. A **370**, 634–640 (1996).
31. R. W. Young, B. J. Green, G. H. Camp, I. G. Gibb, and M. S. Waite, "A transparent thin-film CRT screen of Y_2O_2:Eu with contrast-enhancement layer," Proc. Soc. Inf. Disp. **27**, 139–143 (1986).
32. W. B. Gilboy, "Microtomography with ionizing radiations," Appl. Radiat. Isot. **46**, 689–699 (1995).
33. H. Chrétien, *Calcul des combinaison optiques*, 5th ed. (Masson, Paris, 1980).
34. G. Black and E. H. Linfoot, "Spherical aberration and information content of optical images," Proc. R. Soc. London, Ser. A **239**, 522–540 (1957).
35. *Photometrics*, "Spherical aberration in the photometrics system caused by the camera window," Application Note (Photometrics, Tucson, Ariz., 1990).